RSC Advances

PAPER

Published on 11 August 2026

Cite this: DOI: 10.1039/d6ra05089a

Structure-dependent hot-carrier extraction in gold nanoprism/palladium nanodomain bimetallic nanoparticles

Ziyoda Ganieva,[ab] Dániel Zámbó [a] and András Deák *[a]

Multimetallic nanoparticles represent an important class of material for the manipulation of nanoscale charge-carrier separation that can enable their use in various optoelectronic or catalytic applications. In this work, the optical scattering and emission properties of gold nanoprisms with surface-deposited palladium domains are studied. The size and distribution of the Pd domains are controlled by partially preventing Pd deposition at the prisms' surface with a molecular blocker. As the plasmon damping of the prisms depends on the appearance of new nonradiative decay channels due to Pd deposition, whereas the photoemission of the particles is additionally profoundly influenced by the availability of hot charge carriers, single-particle investigations are utilized to shed light on the role of the secondary metal's nanoscale surface distribution. It is found that for bimetallic particles showing similar plasmon damping properties, the hot-carrier extraction from the plasmonic core is more efficient with small Pd domains distributed over the entire particle surface compared to the case where larger, but fewer palladium domains are present. The findings can contribute to a more rational design and utilization of nanoscale heterosystems aiming at the generation and localized utilization of optically generated charge carriers.

Received 10th June 2026
Accepted 27th July 2026

DOI: 10.1039/d6ra05089a

rsc.li/rsc-advances

Introduction

The development of bimetallic nanostructures has emerged as a rapidly expanding field in catalysis and energy conversion, as their electronic and optical properties can be precisely tuned through composition, morphology, and interfacial design, resulting in superior catalytic or optoelectronic platforms.[1] By integrating a plasmonically active metal such as gold (Au) with a catalytically active metal such as palladium (Pd) or platinum (Pt), hybrid architectures that outperform their monometallic counterparts can be constructed.[2] When, for instance, a catalytic metal is combined with nanoparticles supporting localized surface plasmon resonance (LSPR), additional improvements can be achieved. Such nanostructures are often termed "antenna–reactor" systems, in which the plasmonic component harvests light and concentrates its energy in the electromagnetic near-field close to the particle surface, enabling higher-rate chemical transformations at the catalytic component located at these sites.[3] However, when the plasmonic particle is in direct contact with a metal domain, the energy carried by the plasmon may also be transferred to the secondary metal in additional pathways. In general, plasmon decay takes place through radiative or nonradiative pathways, where for the latter, some charge carriers or excitation energy might be transferred to the surroundings (*e.g.* metal domain), and energetic (hot) charge carriers are generated within the plasmonic nanoparticle itself following the plasmon decay.[4] In bimetallic nanoparticle systems, plasmon-induced direct generation of separated carriers can occur at the metal–metal interface, which serves as a nonradiative damping channel for the plasmon oscillation. This metal–metal interface damping manifests itself as spectral broadening and attenuation of the plasmonic particles' LSPR due to enhanced energy dissipation.[5] The generated hot carriers can transfer from the plasmonic particle to the secondary metal component, also leading to charge separation.[6]

Different plasmonic nanoparticles (*e.g.* rods, prisms) have been successfully combined with Pd or Pt, with the main focus on the implications of the plasmon-determined modulation of the catalytic activity of the secondary metal.[7–10] For exploiting the plasmonic and catalytic properties simultaneously, however, the spatial distribution of catalytic metal on plasmonic nanostructure is an important factor: when the plasmonic particles are coated with a uniform secondary metal shell (core/shell structure), the particles can lose their plasmonic properties due to excessive metal-induced damping and light absorption.[9,11] Hence, the deposition of ultrathin or domain-structured metal adlayers is preferable.[7,8,10] An appealing bottom-up approach for controlling the metal adlayer structure deposited on plasmonic nanoparticles is based on modulating the particles' surface properties by ligand exchange or

[a]HUN-REN Centre for Energy Research, Konkoly-Thege M. út 29-33, H-1121 Budapest, Hungary. E-mail: andras.deak@ek.hun-ren.hu

[b]Chemistry Doctoral School, Faculty of Sciences, University of Pécs, Ifjúság Str. 6, H-7624 Pécs, Hungary

adsorption. It has been shown that the concentration (and sometimes also facet) dependent adsorption of molecules or even simple ions can influence the spatial distribution of the secondary metal domains by modulating the surface availability of nucleation sites during metal deposition.[12,13] Thiol-containing 5-amino-2-mercaptobenzimidazole (AMBI) has already been shown to be effective for inducing domain-like growth of silver or gold on plasmonic nanoparticles by blocking parts of the particle surface.[14–18] The surface distribution of AMBI can be anticipated to be sensitive to temperature during surface modification, as in general both desorption and surface diffusion are thermally activated processes.[19] Hence, while ligand exchange with AMBI is reported in the literature to be carried out routinely at 60 °C, both the concentration of AMBI and the applied temperature can impact the size and distribution of the secondary metal domains, offering a higher degree of control over the properties of the bimetallic heteroparticles.

In this study, we use AMBI to modulate the deposition of Pd on gold nanoprisms. In contrast to nanospheres or rods, such prism-shaped gold particles feature largely different local surface curvature at the faces and sides/tips, which can impact the ordering of the AMBI molecules during ligand exchange. We focus on AMBI surface modification conditions, where a partial coverage of the nanoprisms is ensured. In addition, we modulate the spatial distribution of AMBI on the particle surface by controlling the temperature and ligand concentration during the molecular surface modification step before Pd deposition. Using the deposited Pd domains as reporter entities, we investigate the influence of temperature-dependent AMBI distributions on Pd domain deposition on the particle surface and the effects of the resulting structural variations on the optical properties of the particles. Based on the scattering and photoluminescence spectra of individual particles, the charge carrier separation in the heteroparticles is qualitatively characterized. It is shown that the distribution and structure of the Pd domains profoundly determine the charge separation in such bimetallic nanoparticles, and high coverage is not necessarily required for an efficient charge transfer. The results indicate that with proper structural control in bimetallic nanoparticles, the amount of the catalytic metal can be reduced while still retaining a sufficient intraparticle charge separation.

Materials and methods

Chemicals

Hydrogen tetrachloroaurate trihydrate ($HAuCl_4 \cdot 3H_2O$, 99.9%), cetyltrimethylammonium chloride (CTAC) solution (25 wt% in H_2O), ascorbic acid (AA, 99%), sodium iodide (NaI, 99.5%), sodium borohydride ($NaBH_4$, 99%), AMBI (96%), and palladium(II) chloride ($PdCl_2$, 99.999%) were purchased from Sigma-Aldrich. Ultrapure water (resistivity ≥18.2 MΩ cm) was used in all syntheses, washing steps, and solution preparations. All glassware and magnetic stirring bars were thoroughly cleaned with freshly prepared aqua regia (3 : 1 v/v concentrated HCl : HNO_3), rinsed repeatedly with ultrapure water, and dried at 70 °C prior to use. H_2PdCl_4 solution was prepared by dissolving 0.0037 g $PdCl_2$ in 0.169 mL HCl (37%) under stirring, followed by dilution to a final volume of 10.4 mL with ultrapure water. Moisture- and air-sensitive reagents, including $NaBH_4$, NaI, and AMBI, were stored and handled in a glove-box, and their aqueous solutions were prepared immediately before use.

Preparation and surface functionalization of Au nanoprisms

Synthesis of Au nanoprisms

The nanoprisms were synthesized and purified according to a previously reported method.[20] Briefly, CTAC-stabilized gold seeds were prepared by the rapid injection of freshly prepared $NaBH_4$ (300 μL; 0.01 M) into a 25 μL solution of $HAuCl_4$ and CTAC (final concentrations 0.25 and 93.5 mM, respectively). These seeds were aged for 2 hours to improve the nanoparticle shape yield of the synthesis.[21] The aged seeds were then used to initiate a two-step growth process. The seed solution was diluted by adding 500 μL of seed solution to 4.5 mL of 100 mM CTAC for the intermediate growth. Subsequently, 100 μL of this diluted seed solution was first added to a primary growth solution (9.695 mL) containing CTAC (1.6 mL; 0.1 M), ultrapure water (8 mL), $HAuCl_4$ (40 μL; 0.05 M), NaI (15 μL; 0.01 M), and AA (40 μL; 0.1 M). After fast mixing for a few seconds, 3.2 mL of this mixture was rapidly transferred into a secondary growth solution (41.2 mL) under vigorous magnetic stirring. After a minute, the stirring speed was reduced to 250 rpm, and after an hour, the stirrer bar was removed. The as-synthesized nanoprisms were then purified by two consecutive depletion-based purification steps performed in 140 mM and 125 mM CTAC, respectively, to remove shape impurities. The final CTAC concentration in the purified nanoprism dispersion was set to 50 mM.

Ligand functionalization of Au nanoprisms using AMBI

Prior to ligand functionalization, the optical extinction spectrum of the Au nanoprisms was recorded (initial optical density (OD) of 1.186 at 646 nm). The particle concentration was standardized by adjusting the dispersion to an OD of 1.0 at the dipole plasmon resonance maximum (λ_{max} = 646 nm) using 50 mM CTAC solution. The CTAC concentration was reduced to 0.5 mM by centrifuging the sample and diluting with the necessary amount of pure water first, then adding 0.5 mM CTAC to obtain the starting volume. A stock solution of AMBI was prepared in ethanol (8 mM), and different volumes of this stock solution (*e.g.* 0.25 μL to get 0.5 μM final AMBI concentration) were added to 200 μL of the Au nanoprism dispersion under gentle mixing, where the Au^0 concentration was set to 0.17 mM based on extinction measurement at 400 nm.[22] The mixture was incubated for 2 hours in a temperature-controlled water bath at 40 °C and 60 °C to investigate the effect of ligand treatment temperature on subsequent metal deposition.

Deposition of Pd on Au nanoprisms

4 μL of a 2 mM H_2PdCl_4 solution was added to a 200 μL nanoprism dispersion. This was followed immediately by the rapid addition of 4 μL of a 10 mM AA solution, maintaining a metal

precursor to reducing agent molar ratio of 1 : 5.[23] The reaction proceeded under ambient conditions. The Pd-decorated nanoprisms were purified by centrifugation at 2200 rcf for 5 min, followed by redispersion in ultrapure water. A brief sonication step (10 s) was applied to aid particle redispersion during washing. This washing procedure was repeated as needed to remove excess ligand and residual salts.

Methods

UV-Vis-NIR extinction spectroscopy

Ensemble optical extinction spectra were recorded using a Shimadzu UV-3600i Plus UV-Vis-NIR spectrophotometer. These measurements were used both for routine optical characterization and for adjusting the nanoparticle concentration to an OD of 1.0 at the plasmon resonance maximum prior to AMBI functionalization and Pd deposition.

Scanning electron microscopy

Scanning electron microscopy (SEM) images were acquired using a Zeiss LEO 1540-XB instrument operated at an accelerating voltage of 5 keV. SEM measurements were performed on nanoparticle samples where excess CTAC had been first removed by centrifuging. 1 μL of the sample was drop-cast on 2 × 2 mm^2 Si wafers and dried under ambient conditions. After drying, a gentle rinsing with EtOH was employed to further reduce the organic content.

Single-particle dark-field scattering

Measurements were performed with indium tin oxide (ITO)-coated glass substrates (PGO GmbH, CEC020S, 0.7 mm thickness) that were cleaned by sequential ultrasonication in acetone, isopropanol (IPA), and ultrapure water (15 min each) and 1 minute air plasma cleaning (Harrick PDC-32G). The nanoparticles were deposited onto the cleaned substrates by spin coating. Pristine Au nanoprisms were rinsed with ethanol, while Pd-decorated, AMBI-functionalized samples were rinsed with copious amounts of ultrapure water. All samples were gently dried under a nitrogen stream and gently plasma-treated for 30 s prior to measurement to remove weakly bound surface organic species. Single-particle dark-field scattering measurements were performed using an optical microscope equipped with a dedicated oil-immersion dark-field condenser (Olympus U-DCW, NA = 1.2–1.4) and an IR-enhanced halogen light source (100 W, Olympus U-LH100IR). Scattered light from individual nanoparticles was collected using a 50× objective (Olympus MPlanFLN, NA = 0.8) and projected onto the entrance slit of an imaging spectrometer (Princeton Instruments IsoPlane SCT320) coupled to a PIXIS:400BRX CCD camera cooled to −70 °C. A custom-built measurement control and data acquisition software written in LabVIEW was employed to record single-particle scattering spectra (2 s integration time, averaging 5 spectra). Prior to spectral acquisition, the three-dimensional position (x, y, and focal plane) of each nanoparticle was automatically optimized by the control software to ensure comparability of the measurements. The instrument was intensity-calibrated using a dedicated calibration source (Princeton Instruments) to account for the optical transfer function of the whole setup. The spectra were additionally corrected by subtracting the weak scattering emerging from the ITO itself from a nearby particle-free region under identical experimental conditions. For each nanoparticle, the scattering resonance was determined from the corrected spectrum and fitted using a Lorentzian function to extract the damping (Γ) values and corrected with the bulk damping of gold and the additional contribution originating from the wavelength-dependent interband damping of gold in order to better show the impact of Pd on the damping.[24]

Single-particle photoluminescence measurements

Measurements were performed on individual Au nanoprisms deposited on Schott D263 cover glasses (0.17 mm), chosen for their low background fluorescence and high optical transparency. They were cleaned by ultrasonication in a 2% (v/v) Hellmanex III solution for 15 min, followed by isopropanol (IPA) and ultrapure water (15 min each), and subsequently treated with air plasma to remove residual organic contaminants. Dark-field scattering spectra and photoluminescence spectra were sequentially acquired from the same isolated nanoparticles without repositioning the sample (10–20 particles). For the PL measurements, a 40 mW 532 nm DPSS laser was used (Thorlabs DJ532-40), driven in a temperature-stabilised mount (Thorlabs TCLDM9) by a dedicated controller (Thorlabs ITC 510). The laser was expanded by a fixed magnification beam expander (10×, Thorlabs GBE10-A) and coupled into a microscope using a 50 : 50 beamsplitter. The laser diode current was adjusted to obtain *ca.* 3 mW power before entering the objective. The PL spectrum was measured using the same detection setup as for the dark-field spectra. Acquisition parameters were the same as for the scattering spectra. The emission spectra were background-corrected by subtracting the average PL obtained from three different particle-free regions within the measurement area. No change in the dark-field scattering spectra before and after the PL measurement confirmed that laser irradiation did not induce any change in the particles' structure or morphology.

Transmission electron microscopy

Transmission electron microscopy (TEM), high-angle annular dark-field scanning TEM (HAADF-STEM) and energy-dispersive X-ray spectroscopy (TEM-EDS) measurements were carried out using a Thermo Scientific Themis 200 spherical aberration-corrected microscope operated at an accelerating voltage of 200 keV; image analysis was performed using ImageJ. 200 μL of each colloidal sample was centrifuged at 2200 rcf for 5 min to concentrate the particles and remove excess surfactant. The resulting pellet was gently redispersed in ultrapure water. 1 μL of each concentrated nanoparticle dispersion was drop-cast on a carbon-coated copper grid (Ted Pella) and dried under ambient conditions.

Results and discussion

Ensemble spectroscopy and structural characterisation

The as-prepared gold nanoprisms have an edge length of 70 ± 6 nm (Fig. S1). Based on varying the $PdCl_2$: AA ratio for the Pd deposition onto the as-prepared gold nanoprisms,[25] a 1 : 5 molar ratio was chosen for the Pd coating of the nanoprisms, as this provided the highest Pd domain loading without the formation of large, surface-attached Pd particles (Fig. S2). As shown by the ensemble spectra (Fig. 1a), the as-prepared gold nanoprisms have a resonance wavelength around 650 nm, which is shifted to 700 nm when Pd is directly deposited on them. Additionally, the plasmon peak is significantly broadened, as Pd deposition is generally expected to induce strong plasmon damping.[9] When an increasing amount of AMBI is added (also at room temperature) prior to Pd deposition, this plasmon peak broadening is gradually reduced, indicating a decreasing amount of Pd deposited on the surface. Nevertheless, the resonance wavelength remains almost the same for the AMBI-treated prisms compared to the reference. It has to be emphasized that Pd deposition itself is always performed at room temperature. It is only the AMBI surface modification that is performed at different temperatures, as the temperature-determined distribution of AMBI over the prisms' surface might affect the subsequent Pd domain deposition. Fig. 1b illustrates the effect of elevated temperature (60 °C) set during the AMBI treatment; this specific temperature value is regularly set when AMBI is used to modulate material deposition on metallic nanoparticles.[14–17,26] When the particles are first reacted with an increasing amount of AMBI at 60 °C, the extinction spectra of the Pd-grown particles gradually approach that of the reference sample; that is, the peak wavelength shifts towards 650 nm and also narrows (Fig. S3 compares the effect of temperature at 0.5 μM AMBI concentration). This can be attributed to AMBI increasingly blocking the surface sites where Pd can be deposited. This blocking capability of AMBI is in agreement with earlier results for other (bi) metallic or oxide-semiconductor/gold nanoparticle systems, where AMBI was found to be effective in preventing or modulating the overgrowth of the gold core particle.[14,15,17,27,28] Nevertheless, the extinction spectra reveal that the in-plane localized plasmon resonance of the Au nanoprisms remains observable across all samples, indicating that some collective electron oscillations still persist even after Pd deposition and the increased plasmon damping does not lead to a complete suppression of the dipole plasmon mode.[29] Nevertheless, the interfacial damping caused by the Pd deposition should also depend on the contact area between the metals.[30] Hence, the structure of the Pd-deposited nanoparticles has been investigated by scanning and transmission electron microscopies.

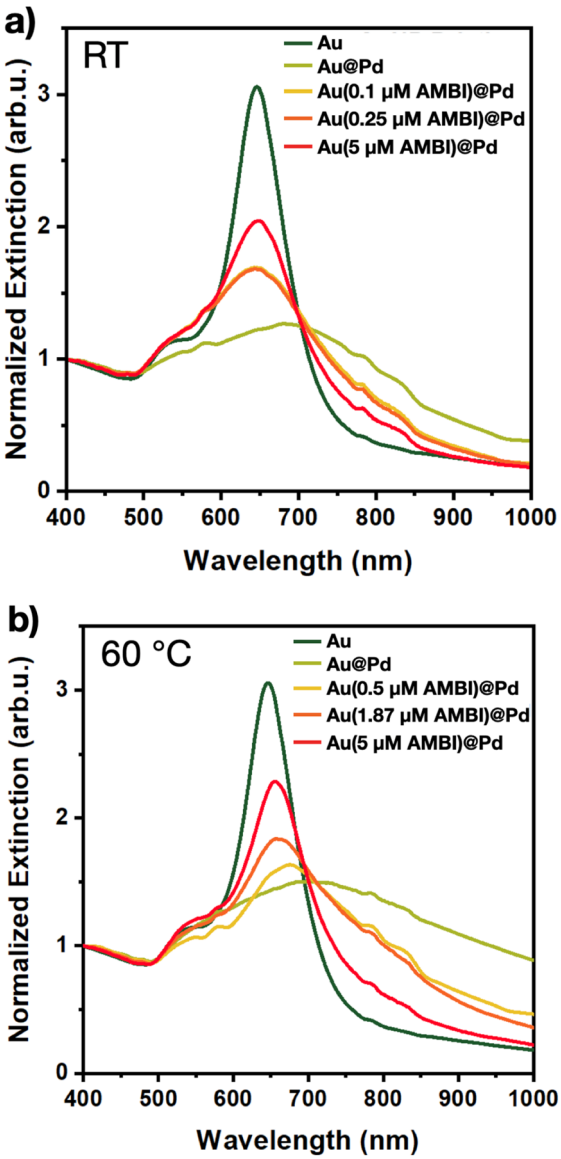

Fig. 1 Ensemble extinction spectra of the Pd domain decorated gold nanoprisms. Different amounts of AMBI are applied at room-temperature (a) and at 60 °C (b) prior to Pd deposition, which is carried out at room temperature in all cases. The spectra are normalized at 400 nm.

Although the overall triangular morphology of the Au nanoprisms is preserved after Pd deposition under all conditions, clear differences in Pd surface distribution are observed (Fig. 2 and S4). In the absence of AMBI, Pd growth appears anisotropic, forming stripe-like or extended domains (Fig. 2a and S4a), consistent with earlier results, where the surface-adsorbed CTAB was found to be directing the development of such patterns.[13,25] The apparent Pd shell wrapped around the perimeter of the prisms shows that the Pd domains also deposit at the edges of the prisms, but otherwise they also cover the face region of the particles (Fig. S4a). Upon introducing AMBI at room temperature (Fig. 2b and S4b), the Pd surface morphology changes, the density of Pd islands decreases and at the same time the individual domains become larger. This behaviour suggests partial passivation of nucleation sites and a redistribution of available growth centres, leading to fewer but more pronounced Pd domains. With increasing temperature during the AMBI treatment (40 °C and 60 °C; Fig. 2c, d, S4c and d), this trend becomes more evident, as also indicated by the increasing size of the Pd domains (Fig. S5). The reduced density of Pd

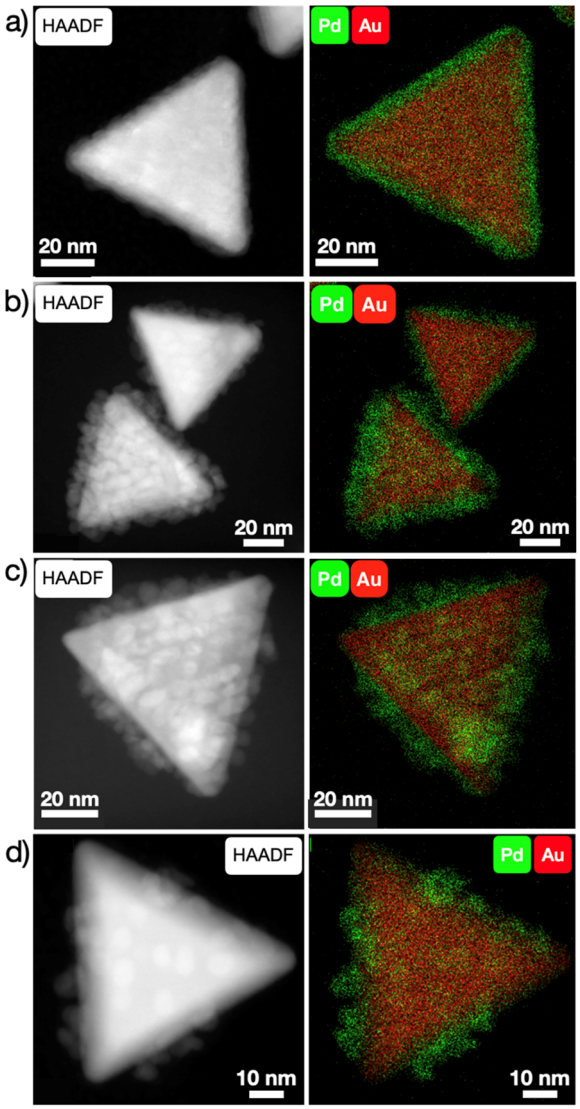

Fig. 2 HAADF TEM images and element composition maps of the Pd deposited Au nanoprisms prepared without AMBI (a) and with AMBI treatment at different temperatures: RT (b), 40 °C (c) and 60 °C (d) prior to Pd deposition. AMBI concentration: 0.5 μM.

islands together with their increased lateral dimensions indicates progressive suppression of accessible nucleation sites, resulting in enhanced growth of existing Pd domains rather than the formation of new ones. The disappearance of the extended stripe features at higher treatment temperatures suggests substantial reorganization or replacement of the initially adsorbed CTAC layer by AMBI. This tendency is consistent with temperature-dependent ligand reorganization, leading to a more stable and densely packed surface layer that limits available nucleation sites for Pd growth.[19] The impact of temperature increase during AMBI treatment on the structure of the Au@Pd particles is corroborated by the image-analysis-derived Pd-coverage decrease (Fig. S5a) and the increase in the TEM-EDS-derived Au : Pd ratio (Table S1).

Single-particle scattering properties

To characterize the impact of Pd deposition and the effect of the AMBI-dictated structural differences of the Pd domain distribution on the optical properties, dark-field scattering measurements were performed on individual Au nanoprisms before and after Pd deposition. To verify the single-particle origin of the spectral data, these measurements were correlated with SEM, and the typical results are shown in Fig. 3 (additional spectra in Fig. S6).

The pristine nanoprisms exhibit a well-defined scattering peak centred around 2.0 eV, corresponding to the characteristic in-plane dipole plasmon mode of the prisms. When palladium is deposited on the nanoprisms (without AMBI), the scattering is extremely damped and an almost featureless spectrum is observed, indicating the dominance of the nonradiative plasmon decay channels. Similar behaviour was observed earlier for gold nanorods decorated with a dense layer of platinum domains and can be attributed to the combined effect of absorption enhancement in the non-plasmonic metal layer as well as to the direct generation of separated charge carriers at the interface between the gold core and the satellite metal domains.[6,29] When AMBI is applied before Pd deposition, however, the dipole resonance feature in the dark-field spectra is partially recovered, irrespective of the temperature during AMBI treatment. Nevertheless, the scattered intensity shows a clear decrease compared to that of the pristine nanoprisms due to the increased total damping.

To clarify in more detail how temperature during the AMBI treatment and hence the resulting varying distribution of the Pd domains affect the optical properties, plasmon damping was determined by fitting the scattering spectra of the ITO-supported particles. In Fig. 4a, the damping values obtained for the different samples are summarized (except for the case where no AMBI was applied, as these spectra are almost featureless). The Pd domains generally increase the interfacial

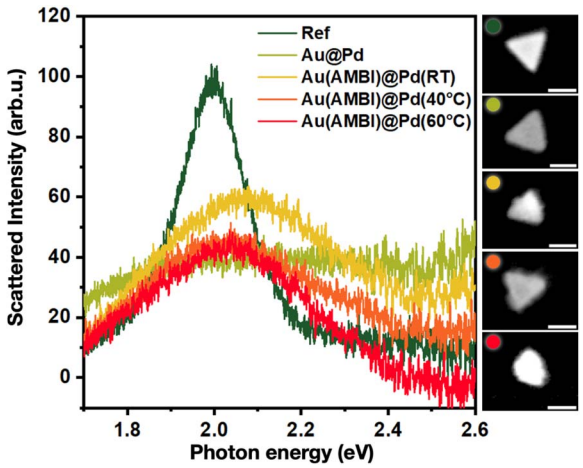

Fig. 3 Correlative single-particle dark-field scattering spectra and SEM images of selected Au nanoprisms without AMBI and with AMBI treatment at different temperatures prior to Pd deposition. AMBI concentration: 0.5 μM. Scale bars: 50 nm.

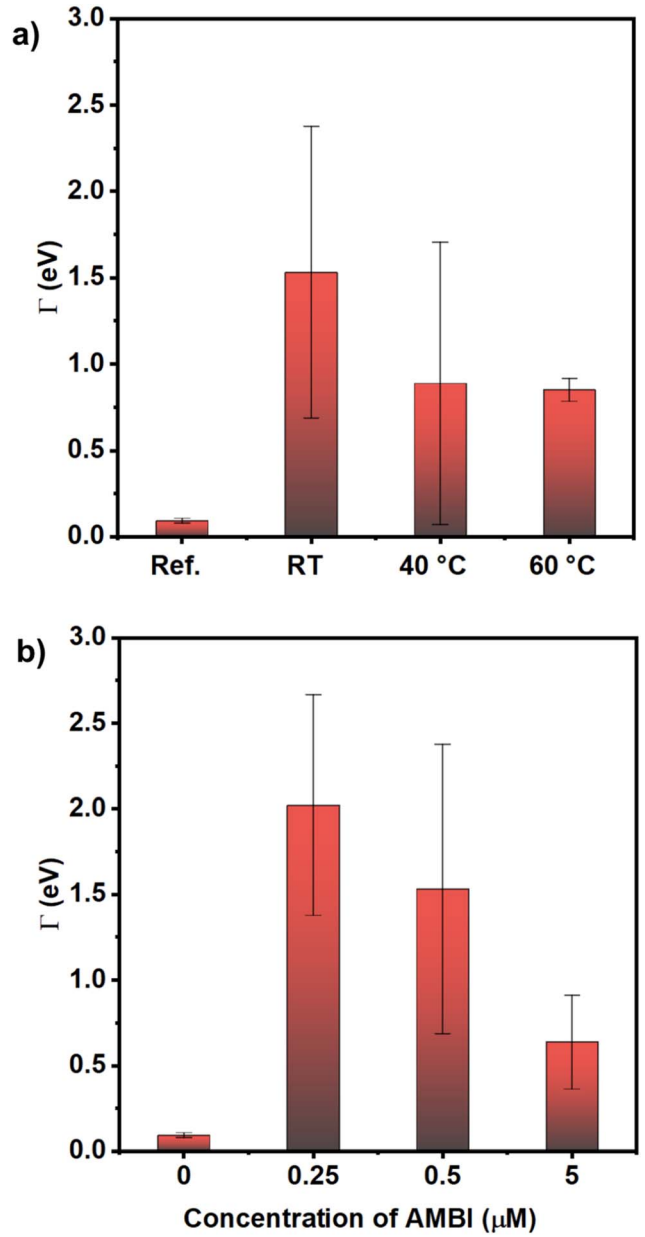

Fig. 4 Single-particle scattering spectrum-derived plasmon damping of the Pd domain-decorated gold nanoprisms showing the impact of temperature applied during AMBI functionalization at a fixed 0.5 μM AMBI concentration ('Ref.' refers to the reference, as-prepared gold nanoprisms without Pd decoration) (a) and the AMBI concentration dependence of the damping for room temperature surface-modified samples ('0' refers to the reference, as-prepared gold nanoprisms without Pd decoration) (b).

damping; their contribution can be assumed to scale proportionally with the coverage of the gold core.[12,30] Clearly, with increasing temperature, the damping decreases. This correlates with the trend observed in the elemental maps in Fig. 2, showing that the presence of AMBI (especially at higher temperatures) reduces the Pd coverage and hence aligns with the concept of contact-area-determined damping change.[29,30] Large variations in the damping were also observed earlier for Pt-coated gold nanorods and were postulated to originate from the actual (random) distribution of the secondary metal domains, especially in the high-intensity near-field regions of the plasmonic core particles.[29] This explanation can be applied to the present system as well, as the combination of AMBI and elevated temperature was previously shown to effectively prevent material deposition at highly curved regions of gold nanoparticles, including both the tips of nanorods and nanoprisms as well.[27,28] This aligns with the elemental maps again, from which a lower Pd coverage of the prism tips can be anticipated, resulting in a smaller particle-to-particle variation for the more AMBI-covered samples. At the same time, for a fixed level of AMBI concentration, an increase of the Pd domain size is observed in general with increasing temperature due to the reorganization of AMBI at the interface (Fig. S4).

Besides the different ordering of the molecules, simply their increasing surface coverage might also result in the same effect, that is, a steady decrease of the damping with increasing AMBI concentration. Modulation of the AMBI concentration at room temperature enabled us to investigate this aspect, as at room temperature, the distribution of the molecules on the particle surface is least affected by temperature. Indeed, it is found that an increasing AMBI concentration in general leads to a decrease in the damping and its variation as a gradually larger fraction of the particle surface is occupied by AMBI molecules prior to Pd deposition (Fig. 4b and S7). It is interesting to note that the average damping value obtained for the largest investigated AMBI concentration (5 μM) at room temperature is comparable with that of the 60 °C sample, where the concentration was an order of magnitude lower (0.5 μM). This underlines the role of elevated temperature, which promotes the ordering of AMBI molecules at the particle surface, leading to a more efficient blocking of the interface during Pd deposition.

Single-particle photoluminescence results

Plasmon damping is associated with the presence of plasmon decay channels under broadband illumination, whereas changes in the photoluminescence of plasmonic particles reflect the recombination of excited charge carriers within the particle. According to the general picture of PL emission from plasmonic particles, the emission originates from the Purcell effect of enhanced emission from radiative recombination of hot carriers.[31] Due to the specific resonance energy of the particles in the present system (around 2 eV), both interband and intraband recombination contribute to the signal. For pristine particles or when the scattering spectrum of the particles is dominated by a clear plasmonic feature, the main contribution to the photoluminescence comes from plasmon resonance-enhanced radiative intraband charge carrier recombination and photoemission.[8] However, when the plasmon resonance is significantly damped, *e.g.*, due to Pd deposition, a decrease in the PL intensity is expected due to the lower escape probability of the photons (related to the increased damping of the plasmon resonance) and the charge-carrier transfer from the gold to the Pd domains, lowering the recombination probability.[8]

For the single-particle photoluminescence investigation, the same Pd-decorated samples have been deposited on borosilicate substrates to reduce background emission, and individual nanoparticles were identified based on their dark-field spectra (Fig. S8). For these borosilicate-supported particles, the dependence of the damping on the temperature and AMBI concentration was identical (Fig. S9) to that previously observed for the ITO-deposited particles. Looking at the PL emission of the particles, it is clear that Pd deposition induces an almost complete quenching of the PL emission irrespective of the set temperature during AMBI treatment (Fig. S10). Such complete PL quenching was already observed earlier for triangular-shaped, platinum edge-only coated gold platelets.[12] For the pristine gold nanoprisms, the PL emission shape agrees well with the dark-field scattering spectrum as expected, but when Pd is deposited on the prisms, a featureless weak emission is only observed that slowly increases towards higher energies (Fig. S11), which can be assigned to the direct re-emission of interband excited charge carriers.[31] It has to be noted that in the dark-field scattering spectrum of the same particles, the LSPR feature is still observed, but the large damping associated with it effectively cancels the emission enhancement. This, combined with the favourable injection of carriers into the Pd domains, leads to PL quenching.

Notably, the PL emission can be partially recovered if the Pd coverage is manipulated (Fig. 5). As mentioned earlier for the ITO-supported samples, AMBI treatment at room temperature with higher (5 μM) thiol concentration results in damping similar to that of the lower concentration (0.5 μM) treatment at 60 °C; hence the impact of the two different Pd coverages on the plasmon resonance can be considered the same. This holds true for the borosilicate-supported particle samples used for the PL measurements as well (Fig. S9). While the damping is similar, the distribution of the Pd domains is different for the 0.5 μM, 60 °C and 5 μM, RT samples. For the 0.5 μM, 60 °C sample, smaller Pd islands are covering the prisms (Fig. S4d); for the 5 μM, room-temperature case, fewer and larger domains can be observed. This structural difference can be attributed to the almost complete blocking of the gold surface by AMBI, allowing only a few Pd domains to grow over the surface. For the latter structure, a significant PL emission is detectable, which is damped compared to the pristine nanoprisms. The scattering spectra of these two AMBI-treated samples are very similar in terms of damping (Fig. 3 and 4), but a clear emission from the prisms with fewer, larger Pd domains can be detected. The comparable damping implies that the Pd-induced non-radiative plasmon decay channels are increased and consequently LSPR-determined emission enhancement decreased similarly for the two cases. Hence, the difference in the emission intensity can be primarily attributed to the availability of hot carriers.

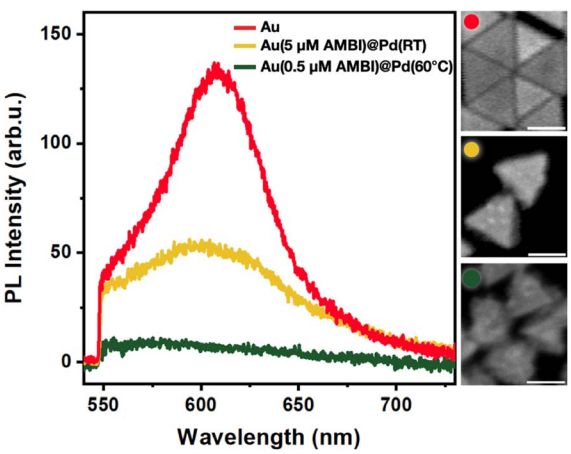

Fig. 5 Typical photoluminescence spectra of the as-prepared and Pd domain-decorated gold nanoprisms with different AMBI surface modification conditions. The insets show characteristic SEM images of the particles. Scale bars: 50 nm.

It was shown earlier that the homogeneous linewidth broadening (damping increase) of the plasmon resonance as derived from single-particle scattering spectra can provide information about the plasmon-induced direct charge injection into the surroundings and that it increases for excitation wavelengths closer to the resonance.[32] For the given two structures, this implies that the plasmon-induced direct charge separation is similar. At the same time, the hot carrier generation inside the particle is larger in higher electric field regions.[33] It is important to emphasize, however, that in the current system, the laser excitation is off-resonant (532 nm excitation wavelength), not favouring the buildup of the in-plane dipolar resonance of the nanoparticles, and the resulting electromagnetic field distribution can be considered more homogeneous compared to a resonant excitation; hence, the spatial distribution of the generated hot carriers is uniform over the particle.[34,35] Hence, for two systems with similar damping, differences in the PL emission intensity should be related to the availability of the hot charge carriers in gold. The PL data indicate that the charge carriers that would otherwise recombine to produce PL emission are much more efficiently extracted from the gold prism into the Pd domains if they are distributed all over the interface due to the higher possibility of electron transfer to a Pd domain before recombination, while having fewer (albeit larger) interfacial domains is less effective in that regard.

Conclusions

In gold nanoprism/palladium domain bimetallic particles, the distribution of the Pd domains has a large influence on the plasmon damping and photoluminescence properties. A thiolated ligand molecule (5-amino-2-mercaptobenzimidazole – AMBI) was used to modulate the distribution of Pd domains over the nanoprism surface, as it can effectively block Pd deposition, provided its local surface concentration is high enough. For below monolayer coverage, both the temperature set during the ligand adsorption and the AMBI concentration were found to be effective parameters to control the Pd domain distribution, which can be attributed to the differences in the packing density of the molecules at the gold prisms' surface. The localised plasmon damping of the gold prisms correlates with the presence of the Pd domains: as the temperature of

AMBI treatment and consequently the patchiness of the Pd domain coverage increases or more blocking molecules are applied, the plasmon damping decreases. This is in accordance with the modulation of the nonradiative plasmon decay by Pd. More importantly, the variation of the AMBI concentration and the temperature applied during the ligand treatment can result in bimetallic particle types featuring similar Pd domain-determined plasmon damping, but with different AMBI particle surface coverage-dictated Pd domain distributions (many smaller *vs.* fewer larger). For these particles showing similar plasmon damping but different Pd domain distributions, a significant difference in the photoluminescence is observed: when fewer but larger domains are present, the PL quenching is less complete, indicating that the presence of numerous 'extraction points' is more favourable for efficient hot charge-carrier separation. The result can be of interest for the rational structural design of plasmonic nanoparticle-based systems, where the nanoscale hot-carrier population is utilized, for example in optoelectronic or catalytic processes.

Author contributions

Conceptualization: A. D.; funding acquisition: D. Z., A. D.; project administration: D. Z., A. D.; supervision: A. D.; methodology: A. D.; resources: A. D, D. Z.; investigation: Z. G., D. Z., A. D.; formal analysis: Z. G., D. Z.; visualization: Z. G., D. Z., A. D.; writing: Z. G, D. Z., A. D.

Conflicts of interest

There are no conflicts to declare.

Data availability

The data for the main-text figures and the measurement settings are available at HUN-REN ARP: https://hdl.handle.net/21.15109/ARP/4HIVYV. The data supporting this article have been included as part of the supplementary information (SI). Additional data are available from the corresponding author upon reasonable request. Supplementary information is available. See DOI: https://doi.org/10.1039/d6ra05089a.

Acknowledgements

Projects OTKA FK 142148 and NKKP Advanced 153064 have received financial support from the Ministry of Culture and Innovation of Hungary from the National Research, Development, and Innovation Fund (NRDI). Z. G. acknowledges the support of the Stipendium Hungaricum PhD Scholarship Program.

References

1 L. Liu and A. Corma, *Chem. Rev.*, 2023, **123**, 4855–4933.
2 L. Ma, S.-J. Ding and D.-J. Yang, *Dalton Trans.*, 2018, **47**, 16969–16976.
3 K. Li, N. J. Hogan, M. J. Kale, N. J. Halas, P. Nordlander and P. Christopher, *Nano Lett.*, 2017, **17**(6), 3710–3717.
4 L. Zhou, Q. Huang and Y. Xia, *Chem. Rev.*, 2024, **124**, 8597–8619.
5 S. A. Lee and S. Link, *Acc. Chem. Res.*, 2021, **54**, 1950–1960.
6 K. Wu, J. Chen, J. R. McBride and T. Lian, *Science*, 2015, **349**, 632–635.
7 Z. Zheng, T. Tachikawa and T. Majima, *J. Am. Chem. Soc.*, 2014, **136**, 6870–6873.
8 G. T. Forcherio, B. Ostovar, J. Boltersdorf, Y.-Y. Cai, A. C. Leff, K. N. Grew, C. A. Lundgren, S. Link and D. R. Baker, *ACS Nano*, 2022, **16**, 12377–12389.
9 A. Roy, D. Paital and S. Khatua, *ACS Appl. Nano Mater.*, 2022, **5**, 4437–4446.
10 L. Ma, S.-J. Ding and D.-J. Yang, *Dalton Trans.*, 2018, **47**, 16969–16976.
11 D. Zámbó, D. Kovács, G. Radnóczi, Z. E. Horváth, A. Sulyok, I. Tolnai and A. Deák, *Small*, 2024, **20**, 2400421.
12 Z. Lou, M. Fujitsuka and T. Majima, *ACS Nano*, 2016, **10**, 6299–6305.
13 P. J. Straney, N. A. Diemler, A. M. Smith, Z. E. Eddinger, M. S. Gilliam and J. E. Millstone, *Langmuir*, 2018, **34**, 1084–1091.
14 Y. Feng, J. He, H. Wang, Y. Y. Tay, H. Sun, L. Zhu and H. Chen, *J. Am. Chem. Soc.*, 2012, **134**, 2004–2007.
15 Z. Wang, Y. Zhou, J. Wang, Y. Wang, J. Zhao, W. Xu and Y. Feng, *ACS Appl. Nano Mater.*, 2024, **7**, 22002–22010.
16 J. Jia, G. Liu, W. Xu, X. Tian, S. Li, F. Han, Y. Feng, X. Dong and H. Chen, *Angew. Chem., Int. Ed.*, 2020, **59**, 14443–14448.
17 T. Jiang, J. Zong, Y. Feng and H. Chen, *Precis. Chem.*, 2023, **1**, 94–99.
18 Y. Feng, Y. Wang, X. Song, S. Xing and H. Chen, *Chem. Sci.*, 2017, **8**, 430–436.
19 J. C. Love, L. A. Estroff, J. K. Kriebel, R. G. Nuzzo and G. M. Whitesides, *Chem. Rev.*, 2005, **105**, 1103–1170.
20 L. Scarabelli and L. M. Liz-Marzán, *ACS Nano*, 2021, **15**, 18600–18607.
21 G. González-Rubio, T. M. De Oliveira, T. Altantzis, A. La Porta, A. Guerrero-Martínez, S. Bals, L. Scarabelli and L. M. Liz-Marzán, *Chem. Commun.*, 2017, **53**, 11360–11363.
22 N. G. Khlebtsov, B. N. Khlebtsov, E. V. Kryuchkova, S. V. Zarkov and A. M. Burov, *J. Phys. Chem. C*, 2022, **126**, 19268–19276.
23 P. J. Straney, N. A. Diemler, A. M. Smith, Z. E. Eddinger, M. S. Gilliam and J. E. Millstone, *Langmuir*, 2018, **34**, 1084–1091.
24 D. Zámbó, D. Kovács, G. Südi, Z. Zolnai and A. Deák, *RSC Adv.*, 2023, **13**, 30696–30703.
25 P. J. Straney, L. E. Marbella, C. M. Andolina, N. T. Nuhfer and J. E. Millstone, *J. Am. Chem. Soc.*, 2014, **136**, 7873–7876.
26 W. Xu, J. Jia, T. Wang, C. Li, B. He, J. Zong, Y. Wang, H. J. Fan, H. Xu, Y. Feng and H. Chen, *Angew. Chem., Int. Ed.*, 2020, **59**, 22246–22251.
27 Z. Ganieva, D. Kovács, Z. Osváth, D. Zámbó and A. Deák, *Adv. Mater. Interfaces*, 2025, **12**, e00512.
28 W. Xu, R. Xiao, S. An, C. Li, J. Ding, H. Chen, H. B. Yang and Y. Feng, *Small*, 2023, **19**, 2300587.

29 A. Joplin, S. A. Hosseini Jebeli, E. Sung, N. Diemler, P. J. Straney, M. Yorulmaz, W.-S. Chang, J. E. Millstone and S. Link, *ACS Nano*, 2017, **11**, 12346–12357.
30 B. Foerster, A. Joplin, K. Kaefer, S. Celiksoy, S. Link and C. Sönnichsen, *ACS Nano*, 2017, **11**, 2886–2893.
31 Y.-Y. Cai, J. G. Liu, L. J. Tauzin, D. Huang, E. Sung, H. Zhang, A. Joplin, W.-S. Chang, P. Nordlander and S. Link, *ACS Nano*, 2018, **12**, 976–985.
32 B. Ostovar, S. A. Lee, A. Mehmood, K. Farrell, E. K. Searles, B. Bourgeois, W.-Y. Chiang, A. Misiura, N. Gross, A. Al-Zubeidi, J. A. Dionne, C. F. Landes, M. Zanni, B. G. Levine and S. Link, *Sci. Adv.*, 2024, **10**, eadp3353.
33 A. Manjavacas, J. G. Liu, V. Kulkarni and P. Nordlander, *ACS Nano*, 2014, **8**, 7630–7638.
34 E. Cortés, W. Xie, J. Cambiasso, A. S. Jermyn, R. Sundararaman, P. Narang, S. Schlücker and S. A. Maier, *Nat. Commun.*, 2017, **8**, 14880.
35 N. H. Kim, C. D. Meinhart and M. Moskovits, *J. Phys. Chem. C*, 2016, **120**, 6750–6755.

